Enhanced Photocatalytic CO_2 Reduction with Defective TiO_2 Nanotubes Modified by Single-Atom Binary Metal Components

Honghui Pan
Huazhong University of Science and Technology
Xiaoguang Wang
Huazhong University of Science and Technology
Zhiwei Xiong
Huazhong University of Science and Technology
Minghui Sun
Huazhong University of Science and Technology
Muthu Murugananthan
Department of Chemistry, PSG College of Technology
Yanrong Zhang (yanrong_zhang@hust.edu.cn)
Huazhong University of Science and Technology

Article

Keywords: Strong Metal Support Interactions, Electron-hole Pairs, Charge-carrier Transmission, Oxidation Path, Self-oxidization

Posted Date: October 28th, 2020

DOI: https://doi.org/10.21203/rs.3.rs-90640/v1

Version of Record: A version of this preprint was published at Environmental Research on July 1st, 2021.
See the published version at https://doi.org/10.1016/j.envres.2021.111176.

Abstract

A binary component catalyst consists of single atoms (SAs- Pt and Au) anchored on self-doped TiO_2 nanotubes (TNTs), was developed for photocatalytic CO_2 reduction. The defects introduced TNTs substrate was stabilized with atomic Pt and Au via strong metal support interactions (MSI), due to which, the covalent interactions of Pt-O and Au-Ti facilitated an effective transfer of photo-generated electrons from the defective sites to the SAs, and in turn an enhanced separation of electron–hole pairs and charge-carrier transmission. The Pt-Au/R-TNTs with 0.33 wt% of SA metals, exhibited a maximum of 149 times higher photocatalytic performance than unmodified R-TNT and a total apparent quantum yield (AQY) of 17.9%, in which the yield of CH_4 and C_2H_6 reached to 360.0 and 28.8 μmol g^{-1} h^{-1}, respectively. The metals loading shifted the oxidation path of H_2O from •OH generation into O_2 evolution, that inhibited the self-oxidization of the photocatalyst.

Introduction

Trapping and recycling of CO_2 by means of photocatalytic route is found to be an effective strategy in coping up with the present challenge of increasing severe greenhouse effect. CO_2 reduction using heterogeneous photocatalysis is a well proven technique because of its ability to directly convert the solar energy into high-value products such as methane, methanol, formaldehyde, formic acid, urea, carbonated vinegar and polymers, etc.[1,2]. However, for a complete realization, efficient adsorption of CO_2 and sufficient energy input are required in activating the linear symmetric CO_2 molecule which is thermodynamically challenging one due to high bond energy (750 kJ/mol) of C=O[3,4]. TiO_2 is widely used for photocatalytic reduction of CO_2 owing to its suitable band structure and efficient photoelectric properties[5]. Besides the reduction of CO_2, water oxidation is allowed to take place that is actually crucial for the conversion of CO_2 into fuel molecules. In spite of all, surface of the TiO_2 is featureless to establish an effective chemisorption with CO_2, that results in CO_2 of high activation energy and extremely poor reaction dynamics[6]. Further, the photocatalytic performance of TiO_2 is being severely limited by inefficient utilization of light source and rapid recombination of photogenerated electron–hole pairs.

Single-atom metal catalysts (SACs) have been of great attraction in the past years due to a maximum utilization of atom efficiency and a well proven catalytic performance[7,8]. Since the adsorption of reactant molecules takes place through the coordinating unsaturated sites, metal single-atom can effectively reduce the activation energy of the reaction[9]. Bringing the advantageous features of SACs and the light utilization ability of the semiconducting metal oxide together are an intriguing approach for realizing high performance and possibly a better activity in the photocatalytic CO_2 reduction process. However, due to the high surface free energy of the single atoms (SAs) metal, they tend to get aggregated during the photocatalytic process[10], thereby a decelerated reactions. The defective substrate supported SAs prevents the migration of metal atoms and stabilizes the active centers, in which the defective sites anchor the SAs metal via the metal-support interactions (MSI), that result in much reduced surface free

energy of the metals and pretty stable defects of the support as well[11,12]. The SAs metal would accept the photo-generated electrons of defective sites and directly trigger the reaction, by which an inhibited charge carrier recombination and in turn an enhanced photocatalytic activity are possible[13]. Furthermore, the MSI of metal-defect is expected to induce substantial electronic rearrangement between the dispersed metal and the support, which would derive new optical and electronic properties[14,15]. Also, the electronic rearrangement could modulate d-band centers and alter the coordination of the metals, which would affect the molecules chemisorption on the catalysts, thus a constant enhancement in the activity could be possible [16,17].

Otherwise, as per theory, due to the indirect relativistic orbital stretching effect (IROSE), the d-electrons of both Pt and Au susceptibly spark chemical reactions compared to that of the other metals[18]. Attempting for a better couple of metal elements, the bimetallic systems such as CuPt, AgPt, AuCu, AuAg, and AuPt would harmonize local electronic structure of active sites, which could obviously exhibit a much more excellent activity towards CO_2 reduction than monometallic systems[19,20]. In spite of these advantages of the bimetallic clusters and nanoparticles, there have been only a few attempts on binary component involving single atom metal as cocatalysts for photocatalytic CO_2 reduction till date. In particular, mechanism of the enhancement observed in the photocatalytic activity is still ambiguous, further, the migration and utilization of photo-generated carriers due to the bonding of each SAs with the support should be investigated.

In this context, to establish a state of art photocatalyst for CO_2 reduction, the defects were introduced into TiO_2 nanotubes thin film initially by an electrochemical self-doping approach, and the atomic Pt and Au were anchored on the defects of the TiO_2 nanotubes support by an electrochemical deposition step. A binary component of Pt and Au deposited SAC having high degree of dispersion and outstanding performance on CO_2 reduction, was fabricated. A series of photo-electrochemical characterization studies indicated that the developed covalent interactions of Pt-O and Au-Ti facilitated an effective transfer of photo-generated electrons from the defective sites to the SAs of Pt, and Au, that led to an enhanced separation of electron–hole pairs and in turn effective utilization of photo-generated electrons for CO_2 reduction. The findings of the present work would afford new possibilities for fabricating a binary SACs and its versatile applications.

Results

Characterization of catalysts.

The morphology and the lattice orientation of the catalysts were characterized by field emission scanning electron microscopy (FE-SEM), High-resolution transmission electron-microscopy (HR-TEM) and X-ray diffraction (XRD) techniques (Supplementary Figures 1-2). Upon self-doping, the anatase TiO_2 nanotube arrays (TNTs) sample was found to be rich with surface OVs and Ti^{3+} defects as seen in our earlier

work[21]. For the metal deposited composite catalysts, no characteristic peaks for both Pt and Au were seen due to high degree of dispersion or trace quantity of the metals[12,22].

It was further characterized by aberration-corrected high-angle annular dark-field transmission electron microscopy (HAADF-STEM) to spot out the supported metal sites of the TNTs. As appeared in Fig. 1a, the bright spots seen on the TNTs are due to a severe aggregation of the Pt and Au that were nanoparticles larger than 2 nm in size, while the aglare bright spots (Fig. 1b) on the lattice surface of R-TNTs, were the atomically anchored Pt and Au, originated from the strong Z-contrast character[23]. As appeared in Fig. 1c of the energy dispersive X-ray spectroscopy (EDS) mapping, the atomic scale Pt and Au were evenly distributed throughout the support. While for the Pt-Au/TNTs, they obviously reflected the aggregated states (Supplementary Figure 3). As listed in Supplementary Table 1, the inductively coupled plasma optical emission spectrometer (ICP-OES) analysis of the composite catalysts, indicated that the mass contents of the Au and Pt in the range of 0.15% to 0.31%.

On account of the high surface free energy, the individual metal atoms are highly mobile and form aggregates during synthetic process[10]. While on the self-doped support of R-TNTs, they would normally get accommodated on the sites of defects, resulted in a decreased quantity of Ti^{3+} and OVs (Fig. 1d).

Interaction between metals and support

As seen in Fig. 2a, a prominent broad protuberance of light absorption, as a result of localized surface plasmon resonance (LSPR) effect of Au[24], was observed for the both Au/TNTs and Pt-Au/TNTs composites in the range of 400~600 nm. While for the Au/R-TNTs and Pt-Au/R-TNTs, the absorption range was shifted upward featurelessly due to the defects but not the LSPR absorption. The LSPR effect of nano-scale Au that exhibits as the absorptive spectrum of near-infrared through the near-ultraviolet was well documented, which is mainly because of intraband transitions between the outermost electrons within the Au 6s1p hybridized atomic orbitals. As the size gets further decreased, the energy level of the hybridized orbitals would gradually get discrete and downward, and eventually merge with Ti atom of the support and lose the resonance feature[25]. Hence, corresponding the LSPR absorption gets gradually weakened and moved toward high energy region, eventually goes disappearing when the size is smaller than 2 nm[26].

In the anatase phase of TiO_2, the vibration modes of Ti-O bonding showed characteristic Raman signals (Supplementary Figure 4) at ~141 (E_g (1)), ~390 (B_{1g}), ~515 (A_{1g}) and ~634 (E_g(2)) cm^{-1}, while introducing the OVs, the length of the bonding was altered, consequently a slight symmetric shift of 4 cm^{-1} was observed for the R-TNTs[27]. Furthermore, the Raman intensity of the Ti-O in Pt-Au/TNTs was significantly enhanced compared to that in TNTs. Under light irradiation, photo-induced electrons generated from nano-size Au, then migrated to TiO_2 and inelastically collided with the electrons presented there, which boosted the vibration of Ti-O and in turn an enhancement of surface Raman scattering[28].

While for SAs modified semiconductor catalyst, the LSPR effect was no longer presented which could be a reason for the similar Raman features observed for both the Pt-Au/R-TNTs and R-TNTs as well.

As seen in the XPS 4f spectrum of the Pt (Fig. 4b) and Au (Fig. 4c), the absorption edge position was located between 0 to +4 valence for Pt^{n+} (n, 0~4) species and 0 to +1 valence for $Au^{\delta+}$ (δ, 0~1) species, respectively. Further, compared to Pt-Au/TNTs, an up-shift 0.34~0.36 eV of bonding energy (BE) was observed for both Pt and Au in the Pt-Au/R-TNTs composite, which was identical with that for monometal supported SACs in Pt/R-TNTs and Au/R-TNTs composites (Supplementary Figure 5). As the size decreased, the core-shell screening between the metal atoms would get weaken, which reflected the increase of core-level BE, namely a final-state effect of the species[29]. On the other hand, characteristic peaks of Ti^{4+}, a negative shift at 0.61 eV in the Ti 2p spectra (Supplementary Figure 6) were observed upon a self-doping treatment. A positive shift of 0.2 eV in the Ti 2p peaks observed for the atomic Pt/Au anchored R-TNT. The bonding between the support and the atomic Pt/Au made the BE shift, which was a concrete evidence for the uniform anchoring of atomic Pt and Au on the support..

Moreover, the normalized L_3-edge X-ray absorption near-edge spectroscopy (XANES) for Pt and Au was presented in Fig. 2d and Supplementary Figure 6, respectively. The observed higher intensity of Pt L_3-edge white line compared to the Pt foil reference as well as a new prepeak (11530~11550 eV) appeared in advance for the SAs Pt-Au/R-TNTs, revealed that atomic Pt in the SAs Pt-Au/R-TNTs was positively charged. Further, the new prepeak should be attributed to the transition of hybridization between Pt 5d and O 2p orbitals[30], therefore, the Pt species should exist as compounds. As far as the normalized Ti K-edge XANES (Fig. 2e), the three prepeaks (4960~4980 eV, inset of the Fig. 2e) observed against both R-TNTs and SAs Pt-Au/R-TNTs, reflected the higher intensity and non-centrosymmetric characteristics unlike for the perfect TiO_2 by which the presence of defects near Ti atom was confirmed. Furthermore, the existence of three Ti–O shells (R = 1.12, 1.54, and 2.12 Å)[31] was confirmed by the fourier transform extended X-ray absorption fine structure (FT-EXAFS) of Ti (Fig. 2f), wherein the length of those bonds for R-TNTs sample was found to be shortened due to the introduction of OVs[32]. Upon anchoring the Pt and Au, two of the shortened Ti-O bondings in the R-TNTs got resumed, the bond length even exceeded for perfect TiO_2, however, since relative instability of the third Ti-O shell (R = 2.12 Å), of which bonding interaction might be substituted by the MSI, a total disappearance of signal was observed. The introduced metals could trap electrons from defects and make bonding with the uncoordinated defects form M-Ti-O or Ti-O-M, by which Ti-O underwent an elongation. It is very clear that the affinity of the defects towards atomic Pt/Au was very high, and the atoms initially located nearby the vacancy, were readily trapped by the defects with lone electron. More specifically, the 5d orbital of Pt caught the electrons from 3d orbital of Ti^{3+} via bridging O, while the 6s orbital of Au directly trapped a single electron from 3d orbital of Ti^{3+}. The defects-associated atoms of both the metals, are largely covalent in nature and tend to form bonding of Pt-O and Au-Ti[33,34]. These results suggested that a uniform dispersion of single atomic scale Pt and Au on the surface of the defected TNTs support, and that reflected in the spectral analysis as unique characteristics.

Photocatalytic reduction of CO_2 and photoelectric properties of the catalysts

To evaluate the performance of the fabricated catalyst composite on CO_2 reduction, several control experiments were initially conducted, that included (i) treating the gaseous mixture of CO_2 and H_2O with the catalyst under dark condition; (ii) irradiating the gaseous mixture without catalyst; (iii) irradiation of the (i) but without H_2O, and (iv) irradiation of the (i) but without CO_2. No hydrocarbons were found to be formed in all the mentioned cases even at an extended reaction period of 3 hours, proving that the sources of carbon and proton were only from the input of CO_2 and H_2O, respectively.

The yields of photocatalytic CO_2 reduction by using the SAs Pt-Au/R-TNTs, Pt-Au/TNTs, and R-TNTs composites under illumination, were shown in Fig. 3a-b and their corresponding products were listed out in Supplementary Table 1. As seen, the products viz. C_2H_6 and CH_4 were formed by the SAs Pt-Au/R-TNTs composite catalyst and their maximum rate of generation were shown to be 28.8 and 360.0 μmol g^{-1} h^{-1}, respectively, for which the corresponding AQYs were of 2.7 and 15.2 % (total value of 17.9%). The photocatalysis of $^{13}CO_2$ isotope labeling further confirmed the reduction products, for which the signals (Fig. 3c) of the isotopic $^{13}CH_4$ and $^{13}C_2H_6$ were seen at m/z=17 and 32, respectively, and their fragment ions were also observed at m/z = 15, 16, 30, and 31[35,36].

A much higher photocatalytic activity towards CO_2 reduction was observed with SAs Pt-Au/R-TNTs composite, for instance, it was 5.5 and 149 times higher than that of Pt-Au/TNTs and R-TNTs, respectively. Interestingly, the synergistic effect was found with a binary combinations of atomic Pt and Au, in which 2 times higher rate of CO_2 reduction was seen compared with the monometallic system (SACs) of either Pt or Au (Supplementary Figure 8) at same quantity (wt. %) of the SAs metal. Also, the reaction of C-C coupling was favored by the SAs Au/R-TNTs thereby a formation of C_2H_6, which was not feasible with SAs Pt/R-TNTs.

Nevertheless, the evolution of hydrocarbon was getting decreased as the cycles increased and the activity of SAs Pt-Au/R-TNTs gradually decreased during the reaction (Supplementary Figure 9a). It has been reported that the salt intermediate products such as $HCOO^-$, HCO_3^-, and CO_3^{2-} get adsorbed preferably on the active sites, which possibly resulted in a deactivation of the photocatalyst[37]. The peaks displayed in the attenuated total reflectance Fourier transform infrared spectra (ATR-FTIR), were attributable to the bending vibrations of carbonate, stretching vibrations of O-H and C-H bonds of the intermediate species that existed after completion of the photocatalysis process, which could possibly block the active sites of the catalytic surface (Supplementary Figure 10). If this was the case, scouring the surface with deionized water should have restored the activity by recovering the active sites, but the restoring was only partial (Supplementary Figure 9b). The deactivation phenomenon might be originated from the sacrificial oxidation of the catalyst caused by photo-induced holes. To verify the self-oxidation step, a control experiment was conducted by replacing the water gas with 10 vol % mixture of CH_3OH/H_2O. Interestingly,

the activity of the photocatalyst was retained with a higher durability for the hydrocarbons yield (Supplementary Figure 9c). The catalyst underwent deterioration by the self-oxidation, thereby a decelerated photo-reduction of CO_2. During the process, -OH groups that terminated on the surface of TiO_2, were oxidized into •OH, which could in turn oxidize the catalyst itself. However, by substituting CO_3^{2-} with –OH, the durability and activity of the photocatalysis were high and stable for at least 4 runs (Fig. 3d) of the process. Because the CO_3^{2-} would get oxidized into O_2 but not the •OH, thus the self-oxidation of the catalyst was controlled[38].

Excluding the slight shift of the energy band gap of the catalysts, the introduction of defects and loading of SAs had major impact of developing an integrally enhanced system for absorption of the light in the visible and near-infrared regions (Fig. 4a), as well as extended lifetime of the carriers. As seen in Fig. 4b, the decay kinetic analysis of the catalysts showed that the longest average fluorescence lifetime of 105.1 ns was from the SAs Pt-Au/R-TNTs, contrast to 55.3, 35.6, and 28.3 ns from the Pt-Au/TNTs, R-TNTs, and TNTs, respectively. And the finding was further substantiated by the steady state photoluminescence emission (PL) measurement and photocurrent studies. Upon introducing the SAs, a clear quenching of the PL emission peak and 3 times higher photocurrent (3.5 mA/cm^{-2}) were observed (Fig. 4c-d), compared to that of R-TNTs. Additionally, in the TiO_2 crystal lattice, valence band (VB) and conduction band (CB) are formed by 2p orbitals of O and 3d orbitals of Ti, respectively. By the loading of SAs metal, the tail of CB induced by Ti^{3+} defects should be replaced by a state of energy gap originated from the bonding of SAs metal with the defects[39,40], thus the photo-generated electrons would directly transfer from O 2p orbital into Pt 5d orbital, or via Ti 3d orbital into Au 6s orbital[40,41]. The MSI that existed between SAs of Pt/Au and the defects had widen the spectrum of absorptive region, extended the lifetime of the carriers and channelized the electron migration from the defective sites into the SAs metals for which could be an excellent electronic collector and in turn an efficient photocatalysis for CO_2 reduction. Furthermore, electrochemical impedance spectroscopy (EIS) for the SAs Pt-Au/R-TNTs (Fig. 4e) showed a representative Nyquist plot with the smallest arc radius among the catalysts under irradiation, the effective charge separation and transfer could also be a cause for the high performance.

Mechanism of CO_2 adsorption and activation

From *in-situ* DRIFTS spectroscopy technique, it observed that the CO_2 molecules got adsorbed on the surface of SAs Pt-Au/R-TNTs while the H_2O molecules were dissociated into hydroxyl group (OH, at 3300~3500 cm^{-1}) at the initial stage. Then, the adsorbed CO_2 interacted with the surface OH groups to form adsorbed carbonate (CO_3^{2-}, 1320 and 1405 cm^{-1}) and bicarbonate (HCO_3^-, 1635 cm^{-1}) (Fig. 9a-b)[42]. During the CO_2 adsorption process, several distinguishable IR vibrating bands were observed at about 1140 and 2078 cm^{-1} corresponding to the species $HCOO^-$ and CO, respectively. It was understood that the catalyst was capable enough of harvesting infrared lights[43], which has been confirmed in the experiments of our ongoing works. Since the elimination of adsorbed species such as OH, CO_3^{2-}, HCO_3^-,

and $HCOO^-$, was not possible by purging the catalyst surface with He gas, the adsorption should be of chemical interactions (Supplementary Figure 11a-b). Then, a vapor mixture of CO_2 and H_2O was fed till reaching an equilibrium of adsorption. Under UV light illumination, the characteristic peaks were observed at around 1040, 1140, 1230, and 2890 cm^{-1} could be ascribed to CH_3O, $HCOO^-$, CH_2O and -CH groups[44] and all these were found to increase with the illumination period (Fig. 9c-d). As the peaks for CO disappeared, it was understood that the species are converted into highly stable intermediates. It is worth noting that, though most of the earlier works have found the carbonates accumulation[45,46], the present study did not encounter any such accumulation due to their facile conversion with the SAs Pt-Au/R-TNTs composite.

Generally, the conversion of CO_2 into $CO_2^{\bullet-}$ is considered as an initiation and a rate-limiting step of the reduction process[47,48]. As shown in Fig. 10a-b, the EPR spectra of TNTs support merely displayed a signal (a_N=14.8 G) corresponding to DMPO-OH. The loading of the Pt and Au attenuated the •OH generation to a higher extent, at the cost of O_2 evolution (Supplementary Figure 12). Owing to the excellent electron collection capability of Pt and Au, a multi-electron reaction could be achieved with the metal-defect associated active sites in the SAs Pt-Au/R-TNTs, by which the oxidation of H_2O changed from one-electron involved •OH generation into four-electrons O_2 evolution[49]. Furthermore, the CO_3^{2-} modified SAs Pt-Au/R-TNTs completely arrested the •OH generation, which was again an evident that the CO_3^{2-} termination controlled the self-oxidation of the catalysts effectively. On the other hand, the signals of DMPO-CO_2 (a_N=15.8 G, a_H=19.0 G) and DMPO-CH_3 (a_N=15.5 G, a_H=22.8 G) were found to be appeared with the loading of Pt and Au (Pt-Au/TNTs) and these were enhanced further with the SAs Pt-Au/R-TNTs. It was very clear that the catalyst modified with atomic scale Pt and Au, promoted the polarizing performance of CO_2 into $CO_2^{\bullet-}$ and protonated the $CO_2^{\bullet-}$ to yield $\bullet CH_3$.

On the basis of the results obtained in the *in-situ* DRIFTS and EPR spectroscopy studies, the mechanism of alkane (CH_4 and C_2H_6) evolution with SAs Pt-Au/R-TNTs was proposed as Scheme 1. At first, a large amount of the CO_2 molecules was adsorbed on the surface of the catalyst and underwent a reaction to produce $CO_2^{\bullet-}$ under illumination (path 1), followed by an addition reaction with H to generate COOH* (path 2)[50], in which the H was from the photocatalytic H_2O splitting. Subsequently, HCOOH*, as an intermediate product, was formed by reduction of the unstable COOH* (path 3). Instead of forming CH_2O* from HCOOH* by bond-breaking, CH_3O_2* should be formed by H addition to the C=O of HCOOH* (path 4), due to the high bonding energy of C-OH. Upon the H accommodation, the C-OH bond of CH_3O_2* was broken to generate CH_2O*(path 5), owing to the lower dehydroxylation energy[51]. Afterwards, CH_3O* was formed by stepwise hydrogenation of CH_2O* (path 6) and further formation of CH_3OH (path 7) or $\bullet CH_3$ (path 8) was possible in the subsequent hydrogenation steps. Comparing the path of CH_3OH generation, the $\bullet CH_3$ formation was predominantly favored by the H_3C-O* bond-breaking, which was evident for the strong interaction of the O (H_3CO-* bond) with the SAs sites and defects of acidic TiO_2 support[52-54]. At

last, CH_4 was produced by the reaction of single $\bullet CH_3$ with H (path 9), while coupling of two $\bullet CH_3$ resulted in C_2H_6 formation (path 10).

$CO_2^* + e^- \rightarrow CO_2^{\bullet -*}$ Path 1

$CO_2^{\bullet -*} + H^+ + e^- \rightarrow COOH^*$ Path 2

$COOH^* + H^+ + e^- \rightarrow HCOOH^*$ Path 3

$HCOOH^* + H^+ + e^- \rightarrow CH_3O_2^*$ Path 4

$CH_3O_2^* + H^+ + e^- \rightarrow CH_2O^* + H_2O$ Path 5

$CH_2O^* + H^+ + e^- \rightarrow CH_3O^*$ Path 6

$CH_3O^* + H^+ + e^- \rightarrow CH_3OH^*$ Path 7

$CH_3O^* + H^+ + 2e^- \rightarrow \bullet CH_3 + OH^*$ Path 8

- $CH_3 + H^+ + e^- \rightarrow CH_4$ Path 9
- $CH_3 + \bullet CH_3 \rightarrow C_2H_6$ Path 10

In summary, a state of the art composite catalyst of SAs Pt-Au/R-TNTs, was developed by anchoring of atomic scale Pt and Au on the OVs of self-doped TiO_2 nanotubes support. The binary components were dispersed on the surface of the catalyst via strong MSI. The as-prepared SAs Pt-Au/R-TNTs with a composition of 0.33 wt % of SAs metals, performed extremely well on the photocatalytic CO_2 reduction, in which the CO_2 molecule was initially protonated to form $\bullet CH_3$, and converted further into CH_4 and a C-C coupled product of C_2H_6 with the AQY of 15.2 and 2.7 %, respectively. The efficiency was about 5.5 and 149 times higher than that of the Pt-Au/TNTs and R-TNTs, respectively. The remarkable performance was ascribed to the significant enhancement in separation of photo-generated electron-hole pairs and charge-carrier transmission by the MSI of Pt-O and Au-Ti covalent bonding. Furthermore, the pathway of photocatalytic H_2O oxidation changed from $\bullet OH$ generation to O_2 evolution upon loading of Pt and Au, resulting in inhibition of the self-oxidization of the photocatalyst. The excellent reproducibility of photocatalytic CO_2 reduction was maintained due to an effective controlling of $\bullet OH$ generation, that has also been achieved by the carbonate termination. The present work takes a step forward in the understanding of light-induced charge transfer processes between SAs metals and semiconductor support. New opportunities of binary SACs for constructing high-performance photocatalytic system can be explored based on the results established in the present study.

Methods

Chemicals.

Titanium foil (99.9% purity, 0.2 mm thickness) was cut into pieces of 1 cm×3 cm. The analytical grade chemicals purchased were viz. Ethylene glycol (EG), Ammonia fluoride (NH_4F), Sodium sulfate (Na_2SO_4), Chloroplatinic acid ($H_2PtCl_6 \cdot 6H_2O$), Chloroauric acid ($HAuCl_4$) and all were used as received, without further purification. Deionized water with a resistivity of 18.25 MΩ cm^{-1} was used for all the experiments carried out in this study.

Preparation of TNTs.

The self-organized TiO_2 nanotubes (TNTs) were prepared by electrochemical anodization technique reported in our earlier work[55]. Titanium foil used in the anodization experiment was thoroughly cleaned by sequential ultrasonication using a mixture of acetone and ethanol, followed by a chemical polishing with a solution containing $HF/HNO_3/H_2O$ at a volume ratio of 1:3:6 for a period of 1 min. It was finally rinsed with deionized water and dried in a nitrogen stream. The well-cleaned Ti foil was anodized with a two-electrode system using Pt mesh as cathode at a constant potential of 60 V for 8 h. The electrolyte used was a mixture of ethylene glycol with 0.25 wt % of NH_4F and 12.5 wt % of H_2O. The gap between the electrodes was fixed as 2.5 cm, and the electrolyte temperature was maintained constantly at 25 °C using a thermostat. The as-prepared TNTs were calcined at 450 °C in ambient air for a period of 2 h, followed by a self-doping process by an electro-reduction step.

Preparation of R-TNTs.

The TNTs, Pt mesh and a saturated calomel electrode (SCE) were served as working, counter and reference electrodes, respectively. The fabrication of reduced TiO_2 nanotubes (R-TNTs) was accomplished by a cathodic treatment of the TNTs foil at a potential of -1.4 V (vs. SCE) under ambient temperature for 10 min in 0.1 M Na_2SO_4 aqueous electrolyte. The R-TNTs was cleaned with deionized water and finally dried at 60 °C.

Preparation of Pt/TNTs.

The metals Pt were incorporated on the self-organized TNTs by a brief square-wave pulse method in which the working electrode employed was either TNTs. The H_2PtCl_6 electrolyte was prepared in a concentration of 0.3 mM, wherein 0.1 M concentration of NaCl was maintained. To achieve Pt/TNTs catalysts, the operating potential was repeated for six runs to step at -0.2 V vs. SCE for 5 s, then back to 0.2 V for 5 s. While for Au/TNTs and SAs Au/R-TNTs catalysts, the operating potential was repeated for six runs either, to step at -0.6 V for 5 s then back to -0.2 V for 5 s.

Preparation of SAs Pt/R-TNTs.

A similar procedure of Pt/TNTs fabrication, was adopted for SAs Pt/TNTs with a replacement of TNTs by R-TNTs support.

Preparation of Au/TNTs.

A similar synthetic procedure of Pt/TNTs, was adopted for the fabrication of Au/TNTs with a change in the operating potential, which was repeated for six runs to step at -0.2 V vs. SCE for 5 s, then back to 0.2 V for 5 s in the 0.3 mM $HAuCl_4$ electrolyte.

Preparation of SAs Au/R-TNTs.

The synthetic procedure of SAs Au/TNTs was similar to Au/TNTs, except for using R-TNTs as support instead of TNTs.

Preparation of SAs Pt-Au/R-TNTs.

The SAs Pt-Au/R-TNTs catalyst was obtained by similar deposition of both Pt and Au for 3 runs each.

Preparation of CO_3^{2-} modified SAs Pt-Au/R-TNTs.

The carbonate modification on the surface of SAs Pt-Au/R-TNTs was carried out by immersing the catalyst in 10 mL of 0.1M Na_2CO_3 aqueous solution for a period of 18 h at 298 K.

Reactor setup and photochemical measurement.

The photocatalytic reduction of CO_2 was carried out in a 15 ml quartz cell reactor with a magnetic stirrer placed at the bottom of the reactor to circulate the gas in it. The photocatalytic film materials were prepared with a dimension of 1 cm × 2 cm. The CO_2 photoreduction was carried out under LED light source (365±10 nm) irradiation and the distance kept between the surface of the photocatalyst and the LED lamp was 1 cm. Before each experiment, the reactor was purged with high-pure CO_2 bubbles through a gas-washing bottle containing aqueous solution for 30 min. And the flow rate of gas was maintained at 50 ml/min. The average irradiation intensity of 365 nm LED (0.208 Wcm^{-2}) was determined by using spectroradiometer. The AQY was calculated by the following equation[56]:

Where [N(Hydrocarbon)×n] and N(photos) are the number of electrons reduced from the CO_2 molecule into hydrocarbon and incident photons, respectively.

The gaseous products were separated in HP-PLOT/Q and MolSieve 5A column, measured by thermal conductivity detector (TCD) and flame ionization detector (FID) with a gas chromatograph system. The TCD temperature was fixed at 200 °C and the oven at 45 °C. The carrier gas used for quantification of H_2, O_2 and CO, was Ar with a flow rate of 4.2 mL min^{-1}. The FID temperature was fixed at 200 °C and the oven at 70 °C. The carrier gas used for the analysis of hydrocarbons was Ar with a flow rate of 10 mL min^{-1}.

The products of CO_2 isotope experiment, viz. CH_4 and C_2H_6, were detected by gas chromatograph-mass spectrometer (GC-MS) equipped with SH-Rtx-wax column. The oven temperature was maintained at 70 °C and the carrier gas was He with a flow rate of 10 mL min^{-1}.

Characterizations

The morphology of the catalysts was analysed by using a FE-SEM operating at an accelerating voltage of 10 kV. HR-TEM images were recorded at an acceleration voltage of 300 keV. The phase and crystal structure of the catalysts were examined by XRD equipped with Cu *K*α radiation (40kV, λ=1.5406Å) and a Raman spectroscopy equipped with an argon ion laser at 532 nm. The optical properties of the catalysts were studied by UV–vis DRS, PL, and ATR-FTIR spectroscopy, techniques. Time-resolved fluorescence emission decay spectra were recorded at 525 nm using excitation with a light pulse of 325 nm by a HORIBA Scientific DeltaPro fluorimeter. By using XPS, the surface elemental analysis were carried out based on the C 1s peak at 285.0 eV. The radical species generated were analyzed by EPR measurement. The metal analysis was carried out by ICP-OES.

Hard XAFS measurement was recorded at the XAS station (BL11) of the Saga Synchrotron Light Research Center, Japan. The Pt and Au L_3-edge XANES data were recorded in a fluorescence mode. The hard X-ray was monochromatized with Si (111) double-crystals. Ti K-edge XANES was recorded in transmission mode.

Electrochemical impedance spectroscopy (EIS) was carried out between 0.1 MHz and 0.01 Hz with 10 mV AC amplitude at −0.05 V DC potential by using an electrochemical station (CHI760E, US) of three-electrode system. The fabricated catalysts, SCE and Pt mesh were fixed as working, reference, and counter electrodes, respectively. The electrolyte used was 0.1 M Na_2SO_4 aqueous solution. A quartz cell was used as reactor for photocurrent test in which 50 mL electrolyte was placed and the reactor set-up was kept 5 cm apart from the 365 nm LED light source. The area of working electrode under illumination was 1 cm^2.

In-situ DRIFTS measurements were conducted by the TENSOR II FT-IR spectrometer equipped with an *in-situ* diffuse-reflectance cell. The reaction chamber was equipped with three gas ports. A mixture of high-pure He, high-pure CO_2, and H_2O vapor could pass into the reaction chamber in which the flux of the target gas (CO_2 and H_2O mixture) and purge gas (He) was controlled by a three-way ball valve system. The chamber has three dome windows, each of which used for separate purpose viz. IR light source, analytical detection, and photocatalyst illumination. And a high pressure mercury lamp was used as UV light source.

References

1. Martín, A. J., Larrazábal, G. O. & Pérez-Ramírez, J. Towards sustainable fuels and chemicals through the electrochemical reduction of CO_2: lessons from water electrolysis. *Green Chem.* **17**, 5114-5130 (2015).
2. Wang, Z. J., Song, H., Liu, H. & Ye, J. Coupling of solar energy and thermal energy for carbon dioxide reduction: status and prospects. *Angew. Chem. Int. Ed.*, **59**, 8016-8035 (2020).
3. Li, K., Peng, B., Peng, T. Recent advances in heterogeneous photocatalytic CO_2 conversion to solar fuels. *ACS Catal.* **6**, 7485-7527 (2016).
4. Xie, S., Zhang, Q., Liu, G. & Wang, Y. Photocatalytic and photoelectrocatalytic reduction of CO_2 using heterogeneous catalysts with controlled nanostructures. *Chem Commun.* **52**, 35-59 (2016).
5. Habisreutinger, S. N., Schmidt-Mende, L. & Stolarczyk, J. K. Photocatalytic reduction of CO_2 on TiO_2 and other semiconductors. *Angew. Chem. Int. Ed.* **2013**, 52, 7372-7408.
6. Li, X., Yu, J., Jaroniec, M. & Chen, X. Cocatalysts for selective photoreduction of CO_2 into solar fuels. *Chem. Rev.* **119**, 3962-4179 (2019).
7. Chen, Y. et al. Single-atom catalysts: synthetic strategies and electrochemical applications. *Joule.* **2**, 1242-1264 (2018).
8. Wang, A., Li, J. & Zhang, T. Heterogeneous single-atom catalysis. *Nat. Rev. Chem.* **2**, 65-81 (2018).
9. Neatu, S., Macia-Agullo, J. A., Concepcion, P. & Garcia, H. Gold-copper nanoalloys supported on TiO_2 as photocatalysts for CO_2 reduction by water. *J. Am. Chem. Soc.* **136**, 15969-15976 (2014).
10. Zhang, H., Liu, G., Shi, L. & Ye, J. Single-atom catalysts: emerging multifunctional materials in heterogeneous catalysis. *Adv. Energy Mater.* **8**, 1701343 (2018).
11. Zhang, J. et al. Cation vacancy stabilization of single-atomic-site $Pt_1/Ni(OH)_x$ catalyst for diboration of alkynes and alkenes. *Nat. Commun.* **9**, 1002 (2018).
12. Wan, J. et al. Defect effects on TiO_2 nanosheets: stabilizing single atomic site Au and promoting catalytic properties. *Adv. Mater.* **30**, 1705369 (2018).
13. Chen, Y. et al. Engineering the atomic interface with single platinum atoms for enhanced photocatalytic hydrogen production. *Angew. Chem. Int. Ed.* **59**, 1295-1301 (2020).
14. Liu, J. Catalysis by supported single metal atoms. *ACS Catal.* **7**, 34-59 (2016).

15. Liu, L. & Corma, A. Metal catalysts for heterogeneous catalysis: from single atoms to nanoclusters and nanoparticles. *Chem. Rev.* **118**, 4981-5079 (2018).
16. Crespo-Quesada, M., Yarulin, A., Jin, M., Xia, Y. & Kiwi-Minsker, L. Structure sensitivity of alkynol hydrogenation on shape- and size-controlled palladium nanocrystals: which sites are most active and selective? *J. Am. Chem. Soc.* **133**, 12787-12794 (2011).
17. Mondelli, C., Gozaydin, G., Yan, N. & Perez-Ramirez, J. Biomass valorisation over metal-based solid catalysts from nanoparticles to single atoms. *Chem. Soc. Rev.* **49**, 3764-3782 (2020).
18. Desclaux, J. P. Relativistic dirac-fock expectation values for atoms with Z=1 to Z=120. *Atom. Data Nucl. Data.* **12**, 311-406 (1973).
19. He, H., Morrissey, C., Curtiss, L. A. & Zapol, P. Graphene-supported monometallic and bimetallic dimers for electrochemical CO_2 reduction. *J. Phys. Chem C* **122**, 28629-28636 (2018).
20. Cheng, M.-J., Clark, E. L., Pham, H. H., Bell, A. T. & Head-Gordon, M. Quantum mechanical screening of single-atom bimetallic alloys for the selective reduction of CO_2 to C_1 hydrocarbons. *ACS Catal.* **6**, 7769-7777 (2016).
21. Wang, X., Sun, M., Murugananthan, M., Zhang, Y. & Zhang, L. Electrochemically self-doped WO_3/TiO_2 nanotubes for photocatalytic degradation of volatile organic compounds. *Appl. Catal. B Environ.* **260**, 118205 (2020).
22. Yang, K. et al. Three-dimensionally ordered mesoporous iron oxide-supported single-atom platinum: highly active catalysts for benzene combustion. *Appl. Catal. B Environ.* **244**, 650-659 (2019).
23. Pennycook, S. J. & Boatner, L.A. Chemically sensitive structure-imaging with a scanning transmission electron microscope. *Nature* **336**, 8 (1988).
24. Villa, A. et al. Characterisation of gold catalysts. *Chem. Soc. Rev.* **45**, 4953-4994 (2016).
25. Alvarez, M. M. et al. Optical absorption spectra of nanocrystal gold molecules. *J. Phys. Chem C* **101**, 3706-3712 (1997).
26. Tsunoyama, H., Ichikuni, N., Sakura, H. & Tsukuda, T. Effect of electronic structures of Au clusters stabilized by poly(N-vinyl-2-pyrrolidone) on aerobic oxidation catalysis. *J. Am. Chem. Soc.* **131**, 7086–7093 (2009).
27. Santangelo, S. et al. Micro-Raman analysis of titanium oxide/carbon nanotubes-based nanocomposites for hydrogen sensing applications. *J. Solid State Chem.* **183**, 2451-2455 (2010).
28. Ding, S.-Y. et al. Nanostructure-based plasmon-enhanced Raman spectroscopy for surface analysis of materials. *Nat. Rev. Mater.* **1**, 16021 (2016).
29. Meyer, R., Lemire, C., Shaikhutdinov, S. K. & Freund, H.-J. Surface chemistry of catalysis by gold. *Gold Bull.* **37**, 1-2 (2004).
30. Lee, M.-C. et al. Hybridized orbital states in spin-orbit coupled 3d–5d double perovskites studied by x-ray absorption spectroscopy. *Phys. Rev. B* **97**, 125123 (2018).
31. Sahoo, M. et al. Nitrogen location and Ti–O bond distances in pristine and N-doped TiO_2 anatase thin films by X-ray absorption studies. *J. Phys. Chem C*, **119**, 17640-17647 (2015).

32. Choi, H. C., Jung, Y. M. & Kim, S. B. Size effects in the Raman spectra of TiO_2 nanoparticles. *Vib. Spectrosc.* **37**, 33-38 (2005).
33. Han, Y., Liu, C.-J. & Ge, Q. Effect of surface oxygen vacancy on Pt cluster adsorption and growth on the defective anatase TiO_2 (101) surface. *J. Phys. Chem. C* **111**, 16397-16404 (2007).
34. Zhang, C., Michaelides, A., King, D. A. & Jenkins, S. J. Structure of gold atoms on stoichiometric and defective ceria surfaces. *J. Chem. Phys.* **129**, 194708 (2008).
35. Liu, Y. et al. Synergetic promotional effect of oxygen vacancy-rich ultrathin TiO_2 and photochemical induced highly dispersed Pt for photoreduction of CO_2 with H_2O. *Appl. Catal. B Environ.* **244**, 919-930 (2019).
36. Sorcar, S. et al. High-rate solar-light photoconversion of CO_2 to fuel: controllable transformation from C_1 to C_2 products. *Energ. Environ. Sci.* **11**, 3183-3193 (2018).
37. Liu, L., Gao, F., Zhao, H. & Li, Y. Tailoring Cu valence and oxygen vacancy in Cu/TiO_2 catalysts for enhanced CO_2 photoreduction efficiency. *Appl. Catal. B Environ.* **134-135**, 349-358 (2013).
38. Teranishi, M., Hoshino, R., Naya, S. & Tada, H. Gold-nanoparticle-loaded carbonate-modified titanium(IV) oxide surface: visible-light-driven formation of hydrogen peroxide from oxygen. *Angew. Chem. Int. Ed.* **55**, 12773-12777 (2016).
39. Zhang, H. et al. Insights into the effects of surface/bulk defects on photocatalytic hydrogen evolution over TiO_2 with exposed {001} facets. *Appl. Catal. B Environ.* **220**, 126-136 (2018).
40. Dong, S., Li, B., Cui, X., Tan, S. & Wang, B. Photoresponses of supported Au single atoms on TiO_2 (110) through the metal-induced gap states. *J. Phys. Chem. Lett.* **10**, 4683-4691 (2019).
41. Wang, C. et al. Ultrahigh photocatalytic rate at a single-metal-atom-oxide. *Adv. Mater.* **31**, 1903491 (2019).
42. Zhang, Z. et al. Support-dependent rate-determining step of CO_2 hydrogenation to formic acid on metal oxide supported Pd catalysts. *J. Catal.* **376**, 57-67 (2019).
43. Liang, L. et al. Infrared light-driven CO_2 overall splitting at room temperature. *Joule*, **2**, 1004-1016 (2018).
44. Ordoño M. B., Urakawa, A. Active surface species ruling product selectivity in photocatalytic CO_2 reduction over Pt- or Co-promoted TiO_2. *J. Chem. Phys.* **123**, 4140-4147 (2019).
45. Wang, Y. et al. CO_2 photoreduction with H_2O vapor on highly dispersed CeO_2/TiO_2 catalysts: surface species and their reactivity. *J. Catal.* **337**, 293-302 (2016).
46. Liu, L., Zhao, H., Andino, J. M. & Li, Y. Photocatalytic CO_2 reduction with H_2O on TiO_2 nanocrystals: comparison of anatase, rutile, and brookite polymorphs and exploration of surface chemistry. *ACS Catal.* **2**, 1817-1828 (2012).
47. Fubini, B., Mollo, L. and Giamello, E. Free radical generation at the solid/liquid interface in iron containing minerals. *Free Rad. Res.* **23**, 593-614 (1995).

48. Park, H., Ou, H. H., Colussi, A. J. & Hoffmann, M. R. Artificial photosynthesis of C_1-C_3 hydrocarbons from water and CO_2 on titanate nanotubes decorated with nanoparticle elemental copper and CdS quantum dots. *J. Phys. Chem. A*, **119**, 4658-4666 (2015).
49. Low, J., Yu, J., Jaroniec, M., Wageh, S. & Al-Ghamdi, A. A. Heterojunction photocatalysts. *Adv. Mater.* **29**, 1601694 (2017).
50. Dimitrijevic, N. M. et al. Role of water and carbonates in photocatalytic transformation of CO_2 to CH_4 on titania. *J. Am. Chem. Soc.* **133**, 3964-3971 (2011).
51. Grabow, L. C. & Mavrikakis, M. Mechanism of methanol synthesis on Cu through CO_2 and CO hydrogenation. *ACS Catal.* **1**, 365-384 (2011).
52. Sakurai, H. & Haruta, M. Carbon dioxide and carbon monoxide hydrogenation over gold supported on titanium, iron, and zinc oxides. *Appl. Catal. A Gen.* **127**, 93-105 (1995).
53. Sakurai, H. & Haruta, M. Synergism in methanol synthesis from carbon dioxide over gold catalysts supported on metal oxides. *Catal. Today* **29**, 361-365 (1996).
54. Subrahmanyam, M., Kaneco, S. & Alonso-Vante, N. A screening for the photo reduction of carbon dioxide supported on metal oxide catalysts for C_1 –C_3 selectivity. *Appl. Catal. B Environ.* **23**, 169-174 (1999).
55. Zhou, H. & Zhang, Y. Electrochemically self-doped TiO_2 nanotube arrays for supercapacitors. *J. Chem. Phys.* **118**, 5626-5636 (2014).
56. Sorcar, S., Hwang, Y., Grimes, C. A. & In, S.-I. Highly enhanced and stable activity of defect-induced titania nanoparticles for solar light-driven CO_2 reduction into CH_4. *Mater. Today* **20**, 507-515 (2017).

Declarations

Acknowledgments

This work was supported by the International Science & Technology Cooperation Program of China (Nos. 2013DFG50150 and 2016YFE0126300) and the Innovative and Interdisciplinary Team at HUST (2015ZDTD027). The authors thank the Analytical and Testing Center of HUST for the use of SEM, TEM, and XPS equipments.

Scheme

Scheme 1 is available in the Supplementary Files

Figures

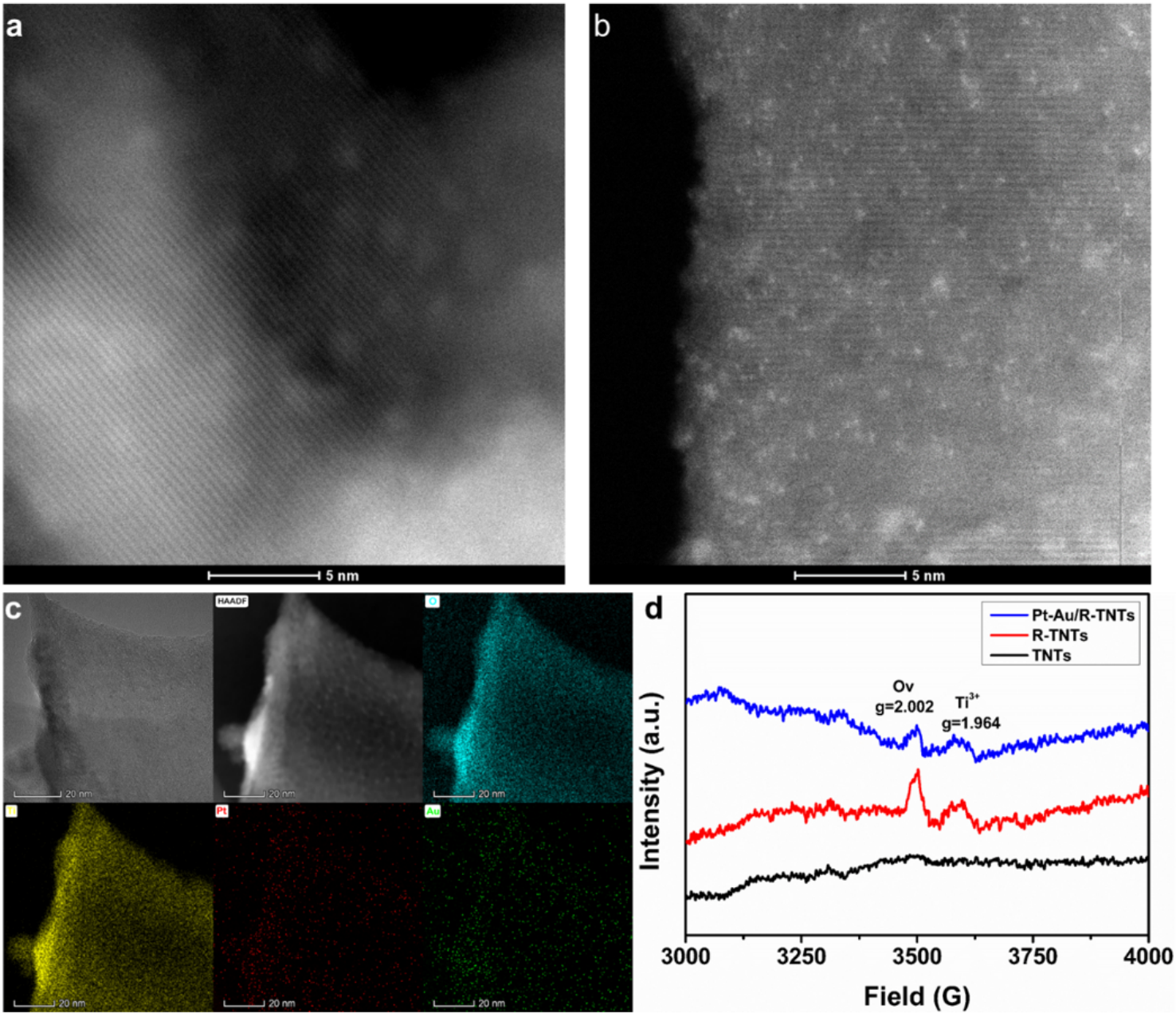

Figure 1

Aberration-corrected HAADF-STEM image of (a) Pt-Au/TNTs and (b) Pt-Au/R-TNTs. (c) Elemental mappings of Pt-Au/R-TNTs display the distribution of O (cyan), Ti (yellow), Pt (red), and Au (green). (d) Electron paramagnetic resonance (EPR) spectra of Pt-Au/R-TNTs, R-TNTs and TNTs.

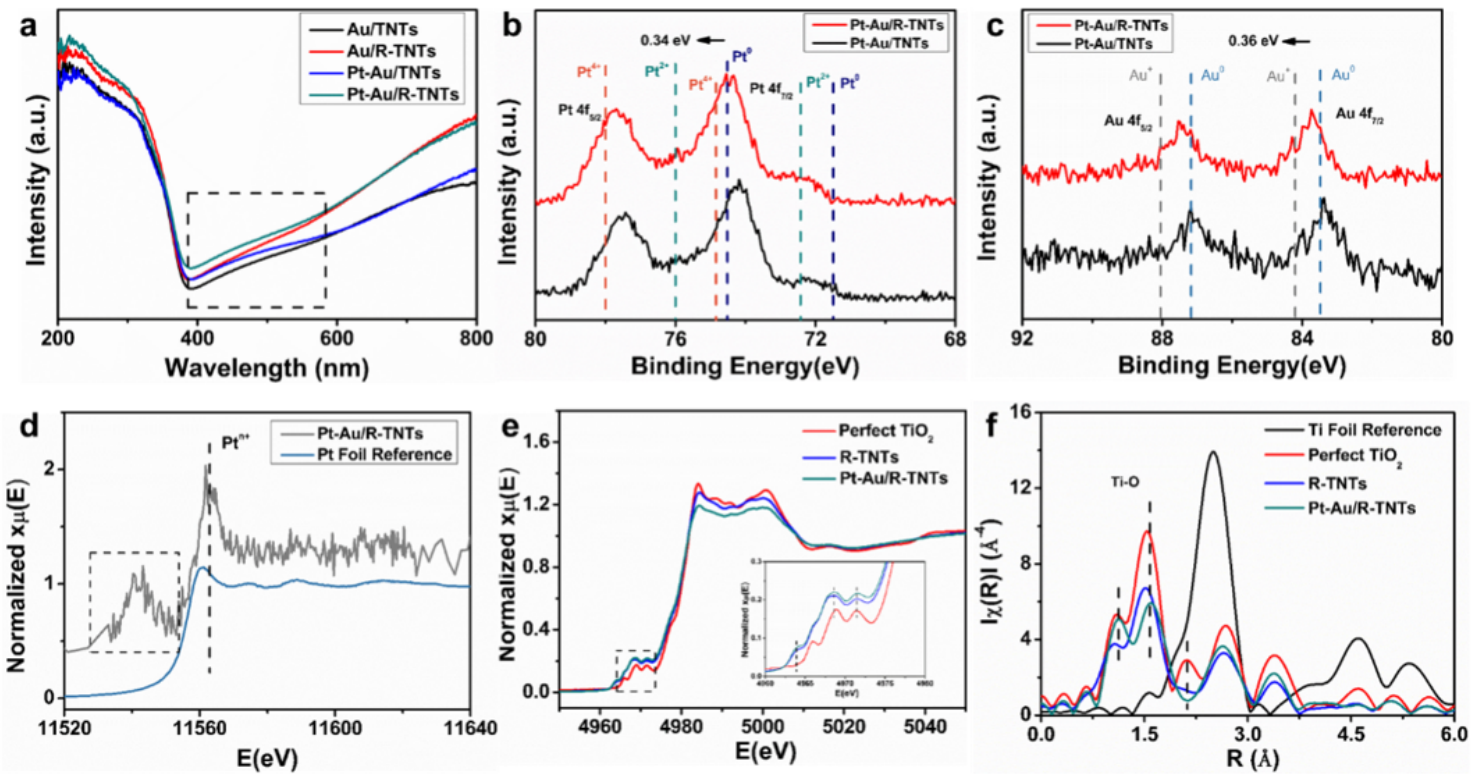

Figure 2

(a) UV–vis DRS of Au/TNTs, Pt-Au/TNTs, Au/R-TNTs, and Pt-Au/R-TNTs. High resolution XPS of (b) Pt 4f and (c) Au 4f spectra in Pt-Au/R-TNTs and Pt-Au/TNTs. XANES spectra of (d) Pt L3-edge and (e) Ti K-edge, (f) FT-EXAFS of the Ti K-edge.

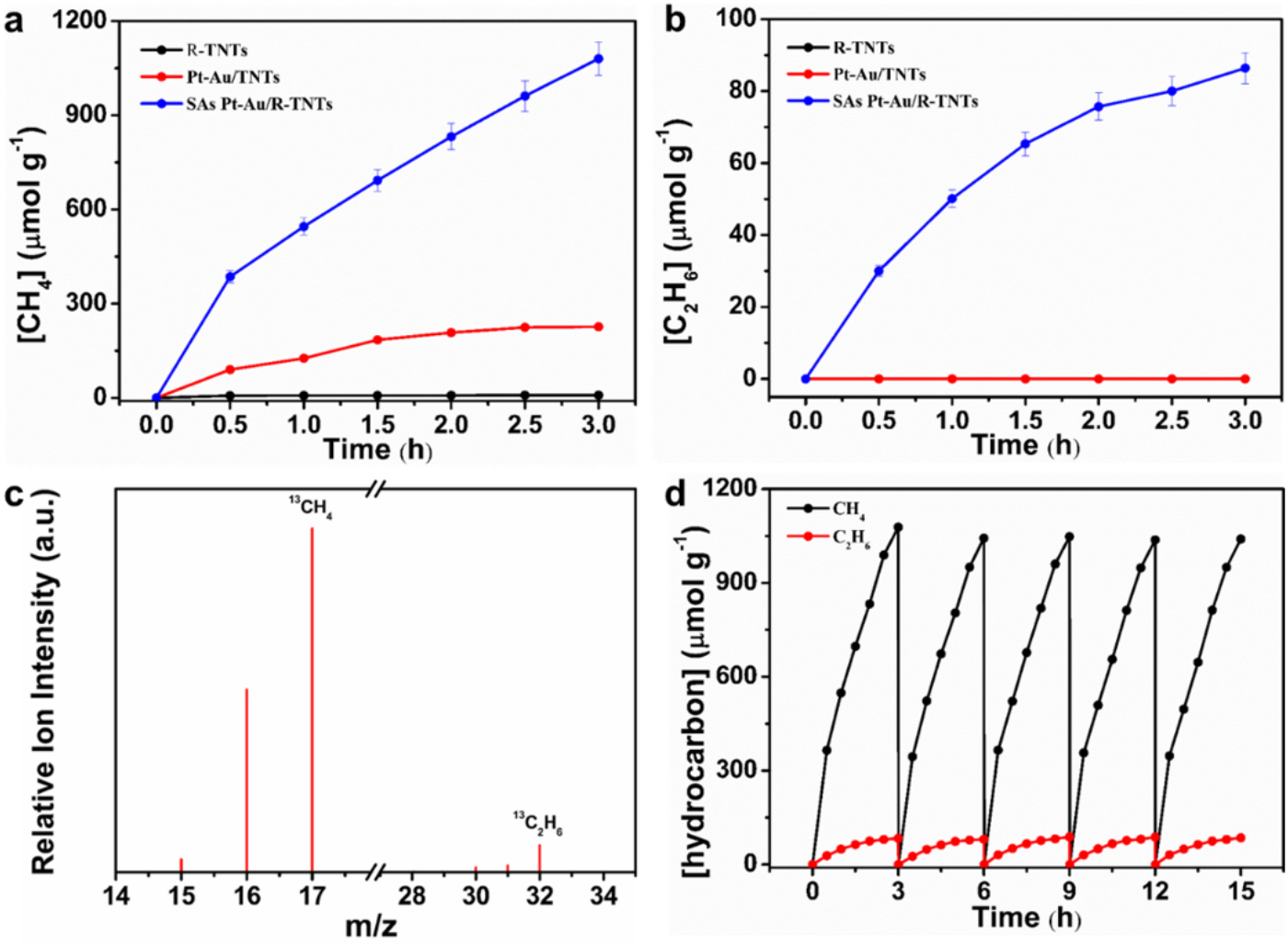

Figure 3

Cumulative evolution of (a) CH4 and (b) C2H6 by SAs of Pt-Au/R-TNTs and Pt-Au/TNTs, and R-TNTs catalysts. (c) MS signals of the 13CO2 isotope labelling experiment. (d) Photocatalytic stability test of the carbonate modified SAs Pt-Au/R-TNTs catalysts.

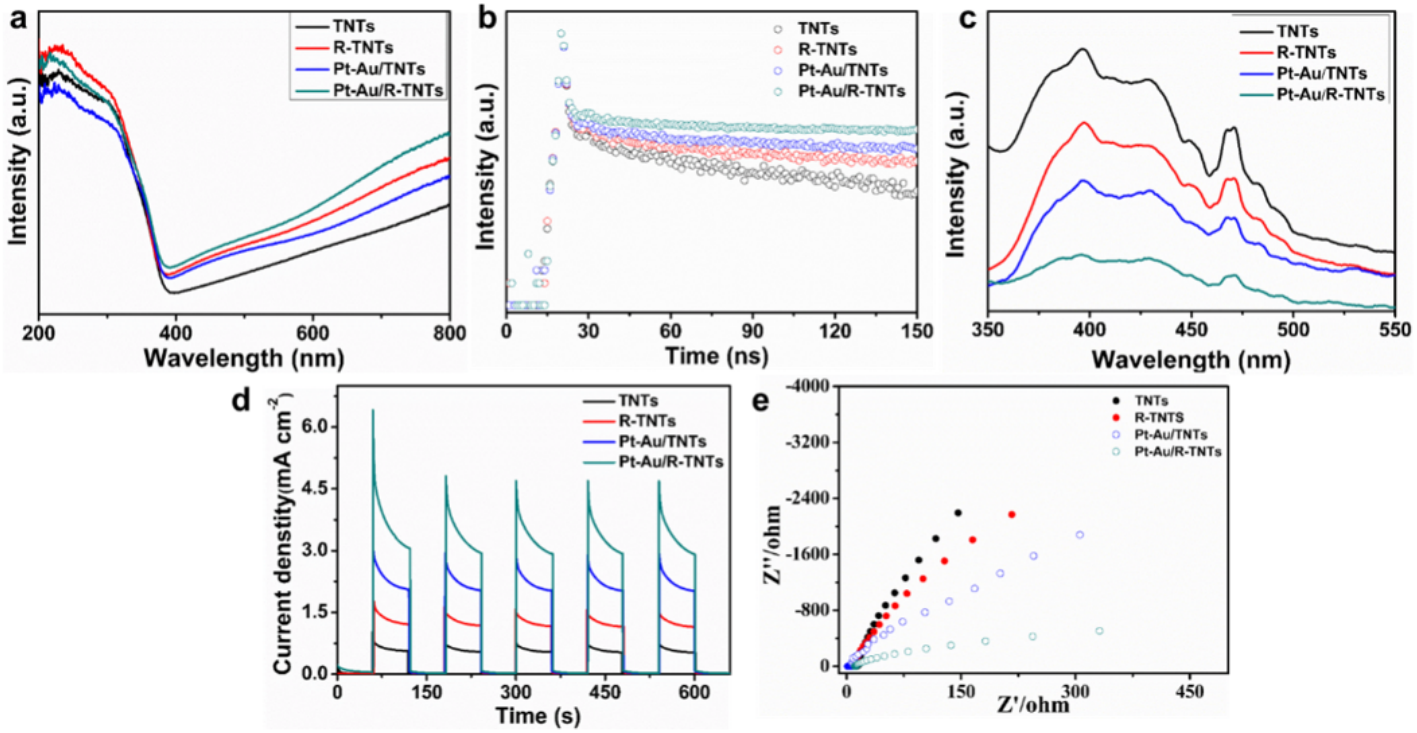

Figure 4

(a) UV–vis DRS, (b) time-resolved fluorescence emission decay spectra, (c) photoluminescence spectra excited at 325 nm, (d) photocurrent curves, and (e) EIS of the fabricated catalysts.

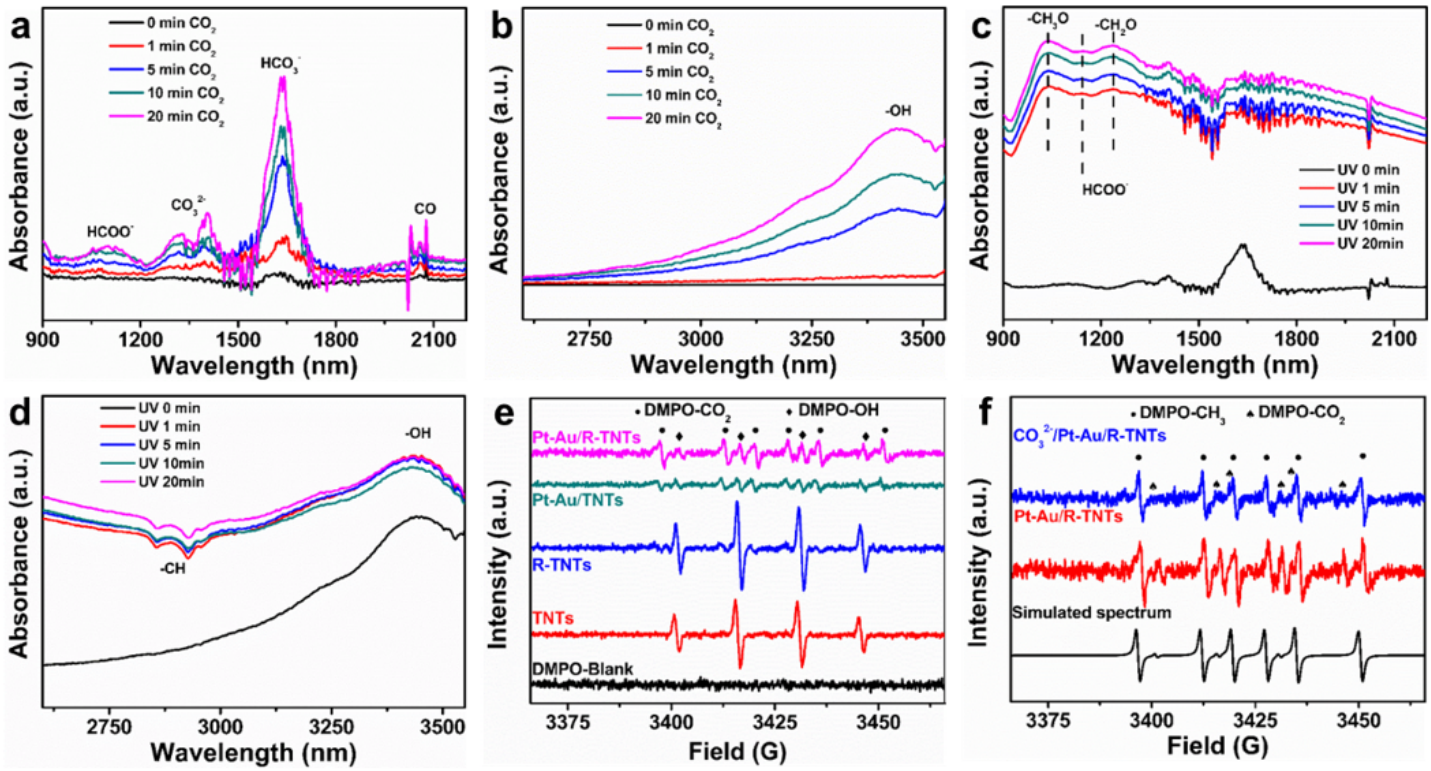

Figure 5

In situ DRIFT spectra of SAs Pt-Au/R-TNTs in CO_2 atmosphere under (a, b) dark condition and (c, d) UV illumination. (e, f) EPR spectra of DMPO−OH, DMPO−CH_3 and DMPO−CO_2 species recorded at room temperature after 3 min of illumination period with UV light.

Supplementary Files

This is a list of supplementary files associated with this preprint. Click to download.

- Scheme1.png
- SupplementaryInformation.docx
- GraphicalAbstract.png